Acta Astronautica 190 (2022) 251–260

Contents lists available at ScienceDirect

Acta Astronautica

journal homepage: www.elsevier.com/locate/actaastro

Research paper

Contribution to the physical description of supercritical cold flow injection: The case of nitrogen

Leandro B. Magalhães [*,1], André R.R. Silva [2], Jorge M.M. Barata [3]

AEROG-LAETA University of Beira Interior, Covilhã 6201-001, Portugal

ARTICLE INFO

Keywords:
Supercritical injection
Liquid rocket engine
Injector heat transfer

ABSTRACT

While increased pressure and temperature contribute to an overall efficiency gain in the mixing of propellants and oxidizers, characteristic of conditions in the combustion chambers of liquid rocket engines, they also propel mixtures to trans- and supercritical conditions. In these conditions, the engine flow exhibits a gas jet-like behavior that may be described using an approach developed for variable density incompressible flows. The present study focuses on an approach using the Reynolds-averaged Navier–Stokes equations to evaluate the jet topology for different injectors' conditions. Based on the so-called 'thermal breakup mechanism concept' proposed in the literature, the axial density decay in supercritical nitrogen jets is predicted for a wide range of conditions. The results show the influence of thermal breakup, providing a better insight of the available experimental data.

1. Introduction

The increasing performance demands of rocket engines have led to conditions in the combustion chamber that exceed the critical point of both the fuels and oxidizers, entering the domain of supercritical fluids. The critical point delimits the supercritical regime and is characterized by pressure and temperature values that become identifiers in the case of pure fluids. Thermodynamic singularities, which refer to the singular behavior of thermodynamic properties at the critical point, need to be accurately replicated in any numerical effort dedicated to the successful description of supercritical fluid behavior. When the isobaric specific heat becomes infinite, the surface tension and latent heat become zero. Besides, the discontinuity between the liquid and gas phases observed at subcritical conditions disappears, resulting in single-phase behavior under supercritical conditions [1]. However, single phase behavior does not imply a uniform behavior across the supercritical regime. In fact, Banuti and Hannemann [2] introduce the concept of thermal disintegration, as complementary to the pure mechanical description of supercritical jet disintegration. The research carried out in this manuscript is built upon the mechanical and thermal disintegration concepts [2].

As a result of the surface tension being zero, finger-like structures would dissolve into the flow [3,4], instead of breaking into several droplets and ligaments. The exact mechanism responsible for the formation of these finger-like structures is not yet understood [5]. Energy dissipation becomes dominant at this point due to the decrease in density, with LES studies [6] demonstrating that the large density gradients between the jet and the chamber environment hinder the development of Kelvin–Helmholtz vortical structures, thus delaying the breakup.

After the critical point is reached, further increases in pressure and temperature may result in the fluid entering the so-called Widom region [7], separating supercritical liquid- and gas-like behavior. Here, several Widom lines have been studied [7–9] as consequences of singularities in different thermodynamic response functions. These can be characterized by a local maxima or an inflection point, as depicted in Fig. 1 for isobaric specific heat (c_p) and density (ρ), respectively. In particular, the response functions associated with the maxima in isobaric specific heat and compressibility are of particular interest [9], as seen in this manuscript.

The Widom region, also labeled as pseudo-boiling in the literature [3,7,10] can be defined as the region where a slight pressure or temperature variation yields a significant response (Fig. 1). Crossing the Widom region from liquid- to gas-like conditions is a similar process to a phase change at subcritical conditions, albeit without the phase change and with the temperature change taking place at a narrow temperature range [10]. The nature of the response was studied by Gorelli

* Corresponding author.
E-mail addresses: leandro.magalhaes@ubi.pt (L.B. Magalhães), andre@ubi.pt (A.R.R. Silva), jbarata@ubi.pt (J.M.M. Barata).
[1] Ph.D. Candidate.
[2] Assistant Professor.
[3] Full Professor.

https://doi.org/10.1016/j.actaastro.2021.09.044
Received 18 February 2021; Received in revised form 3 September 2021; Accepted 30 September 2021
Available online 15 October 2021

et al. [8], who confirmed the relationship between the dynamic and thermodynamic behavior of supercritical fluids at a point well past the influence of the c_p-Widom line. Given that the c_p-Widom line is only visible up to $T_r \approx 3$, the authors consider the minima of thermal diffusivity and kinematic shear viscosity, whose effects are observed for the considered temperature range ($T_r = 4.64$). In this way, Gorelli et al. [8] extend their molecular dynamics computations past the region where the c_p-Widom line effects stop being visible, indicating that a supercritical jet is affected by thermodynamic and dynamic factors.On the other hand, Banuti [10] proposes the transition across the Widom line to be a purely thermodynamic concept, where a pseudo-phase change takes place similar to boiling at subcritical conditions. Between these two interpretations on the nature of the Widom line crossover, Gorelli et al. [8] thermodynamic-dynamic, based on the dynamic response to perturbations and Banuti [10] purely thermodynamic, based on the concept of pseudo-boiling, we follow the theory of pseudo-boiling [10] and is in light of this theory that the results hereby presented should be interpreted.

The effectiveness of a computational method to replicate the behavior of flows under supercritical conditions is dependent upon several factors, ranging from physical models that accurately capture the nonlinear behavior of the various thermophysical parameters, especially in the Widom region, to relevant experimental data for its validation and mathematical models with the ability to simulate the flow behavior. In this way, Reynolds–averaged Navier–Stokes (RANS) and large eddy simulation are validated using the relatively small number of available quantitative experimental data sets [9,11–17]. While the density is retrieved using a real gas equation of state (EoS), the description of derived caloric properties makes use of the departure function formalism. The highly nonlinear behavior [18] in both thermodynamic and transport properties can lead to distinct coupling mechanisms than those observed at subcritical conditions: the inclusion of the Soret and Dufour effects [19–21] in the computations, or of the filtered density in the scope of the EoS [22], may play an additional role. On the other hand, low-pressure turbulence models [23,24] continue to be used [25–27].

Despite the complexities associated to the description of supercritical fluid flows, several advancements have been made in their numerical simulations. Either by considering the flow as compressible [28,29] or taking a variable density but incompressible approach [30], the predictive capabilities of computational methodologies have increased. Aspects of the modeling such as the EoS and the Widom region introduce non-physical pressure oscillations into the flow which need to be dealt with [31–33]. Consequently, entropy stable schemes have been introduced with the objective of improving numerical stability [28], while the production of entropy is used for the flow description [34–36].

RANS [2,27,30,37–40], LES [6,41–44] and direct numerical simulation (DNS) [35,45,46] studies have demonstrated their ability in predicting several features of supercritical jets such as the spreading rate (the importance of which was demonstrated by Chehroudi et al. [47]), mean flow, and thermodynamic properties. The different intrinsic nature of the various numerical and modeling approaches, the definition of grid requirements, as well as difficulties in defining common initial and boundary conditions associated to the interpretation of experimental data [12] remain challenging [48].

Mayer et al. [12] experiments on the injection of single species nitrogen at supercritical conditions remain one of the most comprehensive sources of experimental data for the characterization of supercritical flow behavior. Indeed, Mayer et al. [12] experiments are used extensively for the validation of numerical solvers [2,5,6,25–29,35,37,38,41–45]. While the focus has been on demonstrating models suitability for the description of liquid- and gas-like supercritical behavior, generally, only cases 3 and 4 (Fig. 1) are computed. Moreover, the experimentally measured temperature values [12] seemed to indicate considerable heat transfer from the injection system would affect the jet development. However, heat transfer inside the injector is usually neglected in the computations [5,28,41,43,45].

Table 1
Experimental conditions (Mayer et al. [12]).

Case	Calculated velocity ($m\,s^{-1}$)	Measured chamber pressure (MPa)	Measured temperature T (K)
3	4.9	3.97	126.9
4	5.4	3.98	137.0
7	4.5	5.01	126.2
8	4.9	5.00	135.7

Banuti and Hannemann [2], introduce the concept of thermal disintegration, to complement the mechanical description of supercritical jets. In this way, the authors are able to demonstrate the amount of energy a supercritical jet receives [10] in the injector will determine if a change from liquid- to gas-like conditions takes place, influencing the jet development. With the introduction of thermal disintegration [2], it was possible to evolve from the purely mechanical description of supercritical jets, where a potential core would always be recovered as the jet discharged into the chamber to the retrieval of a disintegrated core (case 4 in Fig. 1), given the pseudo-boiling power, as computed by Banuti and Hannemann [2]. These results were later confirmed by Lapenna [49] with DNS.

In the present work, we aim at extending Banuti and Hannemann [2] conceptualization to a broader range of conditions. Several experimental test cases are considered to validate the computational approach, where it is possible to observe the effect of heat transfer in the injector as the trigger for the pseudo-phase change.

The remainder of this manuscript is organized as follows. First, the test conditions for which there are experimental data available are presented, and previous computational studies using different methods are reviewed, allowing us to position our choices in terms of the state of the art. The mathematical/physical models that constitute the backbone of the RANS approach are reviewed and explained to ascertain their performance, advantages and disadvantages and the role they play in the overall process. Numerical results are presented for liquid- and gas-like injection configurations, detailing the effect of pressure on the phenomena associated with pseudo-boiling. Finally, the main findings are summarized in the conclusions.

2. Review of the experimental conditions

The experimental conditions of Mayer et al. [12] have become the canonical case for validating computational methods that aim at predicting supercritical fluid behavior. To date, it remains the most comprehensive database for single-species injection at supercritical conditions. The injection of a single supercritical liquid nitrogen jet into a chamber filled with gaseous nitrogen is considered, according to the conditions of Table 1.

The experimental study used Raman scattering to measure the axial evolution of density and to evaluate the spread of variable-density jets.

The experimental test conditions are graphically represented in Fig. 1. Variations of density, ρ, and isobaric specific heat capacity, c_p, with temperature, T, are represented for nitrogen, with the experimental data available from the National Institute of Standards and Technology (NIST) database [50]. The test cases correspond to pressures of 4 and 5 MPa and the measured temperatures of Table 1.

Uncertainties in the measured values of the injection temperature [12] need to be discussed, since they have a profound impact on the jet evolution at the considered conditions. The experimental temperature in Mayer et al. [12] experiment was not controlled in an accurate way, due to the complexity of the piping system. For example, the temperature at the injector's exit was measured during a separate measurement campaign. In addition, the heat transfer from the injection system (particularly in the injector) is usually neglected

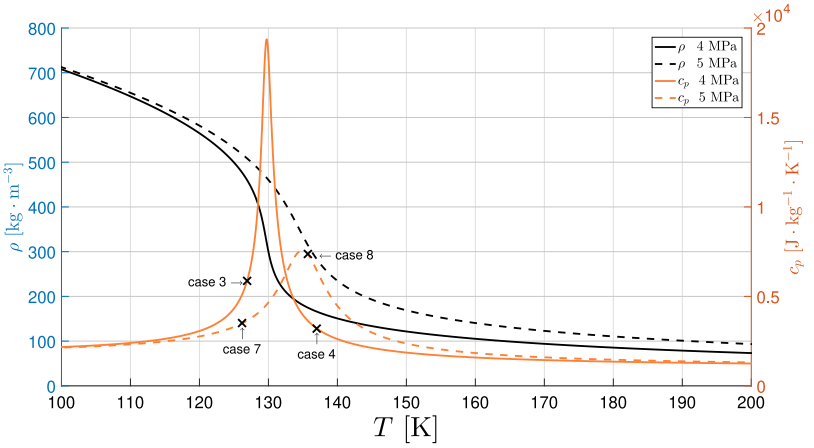

Fig. 1. Experimental data distribution in relation to the pseudo-boiling point.

in the computations, despite indications of its importance. Banuti and Hannemann [2] critically reviewed the influence of temperature uncertainty measurement in several cryogenic experiments, focusing on the neglected injector heat transfer. However, it is still necessary to define an injection temperature and its influence on the results. In Fig. 1, considering the density decay for nitrogen for the 4 and 5 MPa it is possible to observe that a small variation in the injection temperature will result in a large variation in density, especially for case 3, where the steepest slope of density is registered. Given the uncertainties surrounding the injection temperature, any numerical results comparison an absolute match with experiments cannot be sought. Instead a qualitative description, and comparison with the experiments is desired.

In what the injection temperature concerns, this is not the only interpretation. For example, Müller et al. [44], use the density values close to the injector are used for the determination of injection temperature of case 3.

In the present work the inclusion of injector heat transfer, as introduced by Banuti and Hannemann [2] is considered.

The computational domain corresponding to the experimental setup of Mayer et al. [12] is represented in Fig. 2, detailing the boundary conditions (BCs). The chamber and the injector have diameters of 122 mm and 2.2 mm and lengths of 250 mm and 90 mm, respectively. A constant axial velocity profile is set at the inlet, while the radial component is set to zero. At the chamber and injector walls, both the normal and tangential components of velocity are set to zero. A pressure outlet is defined with a gauge pressure of 0 MPa. For comparison purposes, adiabatic and isothermal injector wall configurations are tested. For the adiabatic configuration, along the face-plate, the heat flux is zero, while for the isothermal walls of the injector and chamber, a constant temperature of 298 K is applied [2].

3. Mathematical and physical models

This section presents the conservation of mass, momentum, and energy, and a suitable formulation for a turbulence model. Real gas behavior is accounted for with the inclusion of a real gas EoS and a suitable model for describing the transport properties. Finally, the system of partial differential equations is discretized following a finite volume method, and the solution algorithm is introduced with emphasis on its range of validity and limitations.

3.1. Governing equations and turbulence modeling

An incompressible but variable-density approach is used. The simplification of incompressible but variable-density jet was an hypothesis that came out from the similarity of visualization data and tested for supercritical conditions [30].

The Favre-averaged conservation principles of mass, momentum, and energy are represented in Eqs. (1), (2), and (3), respectively. In these equations, x_j represents the Cartesian coordinates, ρ is the density, u_i and u_j are the velocity components in directions i and j, h is the enthalpy, p is the pressure, τ_{ij} is the viscous stress tensor, and q_j is the heat flux.

$$\frac{\partial \overline{\rho}}{\partial t} + \frac{\partial \overline{\rho}\tilde{u}_i}{\partial x_i} = 0 \tag{1}$$

$$\frac{\partial}{\partial t}\left(\overline{\rho}\tilde{u}_i\right) + \frac{\partial}{\partial x_j}\left(\overline{\rho}\tilde{u}_i\tilde{u}_j\right) = -\frac{\partial \overline{p}}{\partial x_i} + \frac{\partial \overline{\tau_{ij}}}{\partial x_j} - \frac{\partial \overline{\rho}\widetilde{u_i'' u_j''}}{\partial x_j} \tag{2}$$

$$\frac{\partial \overline{\rho}\tilde{u}_j\tilde{H}}{\partial x_j} = \frac{\partial \overline{\tau_{ij}u_i}}{\partial x_j} - \frac{\partial \tilde{u}_i\overline{\rho}\widetilde{u_i'' u_j''}}{\partial x_j} - \frac{\partial\left(\overline{q}_j + \overline{\rho}\widetilde{u_j'' h''}\right)}{\partial x_j} \tag{3}$$

The Reynolds stress tensor, resulting from the averaging process, is given by Eq. (4), as approximated by the Boussinesq hypothesis of Eq. (5), where κ is the turbulence kinetic energy, μ_t is the eddy viscosity, and δ_{ij} is Kronecker's delta function.

$$\overline{\tau_{ij}} = -\overline{\rho}\widetilde{u_i'' u_j''} \tag{4}$$

$$-\overline{\rho}\widetilde{u_i'' u_j''} = -\frac{2}{3}\rho k\delta_{ij} + \mu_t\left(\frac{\partial \tilde{u}_i}{\partial x_j} + \frac{\partial \tilde{u}_j}{\partial x_i} - \frac{2}{3}\frac{\partial \tilde{u}_k}{\partial x_k}\delta_{ij}\right) \tag{5}$$

The turbulence heat flux, $\overline{\rho}\widetilde{u_j'' h''}$, is modeled according to Eq. (6), where Pr_t is the turbulent Prandtl number expressing the ratio of the eddy diffusivity of momentum to the eddy diffusivity of heat.

$$\overline{\rho}\widetilde{u_j'' h''} = -\frac{c_p\mu_t}{\mathrm{Pr}_t}\frac{\partial \tilde{T}}{\partial x_j} = -\frac{\mu_t}{\mathrm{Pr}_t}\frac{\partial \tilde{h}}{\partial x_j} \tag{6}$$

The system is closed by the standard κ–ϵ turbulence model of Ref. [51], where the velocity and length scales are determined from field equations. Eddy viscosity is evaluated from Eq. (7), where κ (Eq. (8)) represents the turbulence kinetic energy and ϵ (Eq. (9)) its dissipation. The turbulence model constants are defined as $\sigma_\kappa = 1.0$, $\sigma_\epsilon = 1.3$, $C_\mu = 0.09$, $C_{\epsilon 1} = 1.44$ and $C_{\epsilon 2} = 1.92$.

$$\mu_t = C_\mu\frac{\overline{\rho}\kappa^2}{\epsilon} \tag{7}$$

$$\frac{\partial}{\partial x_i}\left(\overline{\rho}\tilde{u}_i\kappa\right) = \tau_{ij}\frac{\partial \tilde{u}_j}{\partial x_i} - \overline{\rho}\epsilon + \frac{\partial}{\partial x_j}\left[\left(\mu + \frac{\mu_t}{\sigma_\kappa}\right)\frac{\partial \kappa}{\partial x_j}\right] \tag{8}$$

$$\frac{\partial}{\partial x_i}\left(\overline{\rho}\tilde{u}_i\epsilon\right) = C_{\epsilon 1}\frac{\epsilon}{\kappa}\tau_{ij}\frac{\partial \tilde{u}_j}{\partial x_i} - C_{\epsilon 2}\overline{\rho}\frac{\epsilon^2}{\kappa} + \frac{\partial}{\partial x_j}\left[\left(\mu + \frac{\mu_t}{\sigma_\epsilon}\right)\frac{\partial \epsilon}{\partial x_j}\right] \tag{9}$$

The turbulence closure used in our formulation corresponds to the standard version of the κ–ϵ model from Ref. [51]. As this is not valid

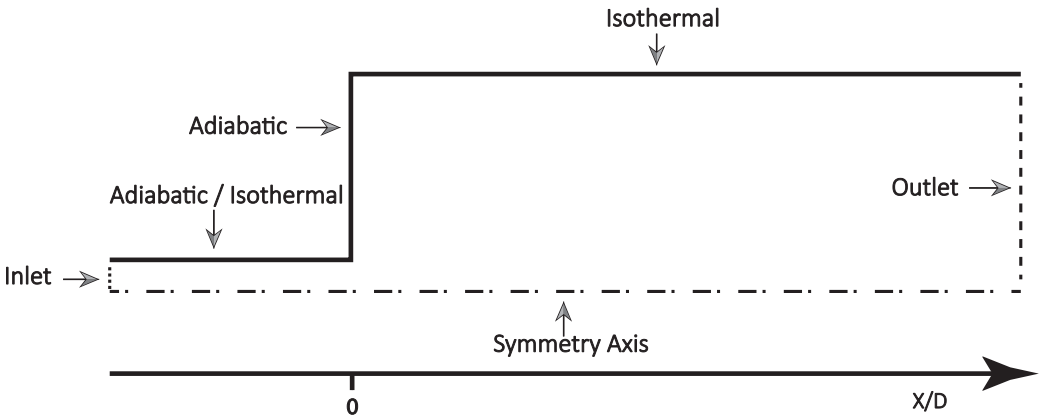

Fig. 2. Boundary conditions.

up to the solid wall, the turbulence model needs to be calibrated according to the wall functions to ensure that the boundary layer is properly resolved. Consequently, wall function modeling bridges the gap between the region affected by viscosity and the fully turbulent region, in which the κ–ϵ model can be applied. Therefore, a y^+ value of 11.63 was considered for the first cells adjacent to the walls. Below this value, the flow was assumed to be purely viscous; above this value, it was considered to be purely turbulent. As well as the y^+ value, there is a need to define a minimum number of points in the mesh that are located inside the boundary layer. Typically, around 20 points are taken to be inside the boundary layer, and so this value was employed in our study.

Both the y^+ restrictions and the minimum number of grid points in the boundary layer are fixed parameters that need to be maintained during the mesh refinement process and the testing of different grid configurations. Other regions will experience higher gradients of thermophysical properties, or will be more influenced by the BCs. In this sense, the injector region and the jet centerline require a higher concentration of cells than the rest of the computational domain during the refinement process.

The initial conditions for κ and ϵ are set according to Eqs. (10) and (11), where l is the characteristic length scale, taken to be equal to the injector diameter, and I is the turbulence intensity, set to 5% in accordance with a preliminary study.

$$\kappa_0 = \frac{3}{2}\left(Iu^2\right) \tag{10}$$

$$\epsilon_0 = \frac{c_\mu^{3/4}\kappa^{3/2}}{0.014l} \tag{11}$$

3.2. Equation of state

The departure from ideal gas behavior paves the way for implementing a real gas EoS. These can be cubic EoSs or more complex formulations explicit in the Helmholtz energy. Cubic EoSs such as the Peng–Robinson (PR) [52] or Soave–Redlich–Kwong [53] expression are often used due to the compromise they represent between accuracy and simplicity. More complex multi-parameter EoSs have also been employed [54], using a modified Benedict–Webb–Rubin equation [2] or formulations based on the Helmholtz energy [27]. In these last two EoS groups, the EoS is solved before the computations, effectively removing the associated computational load on the numerical solver. Tables are then compiled, from which the values of interest can be retrieved during the iterative procedure.

For the present study, the PR [52] EoS [Eq. (12)] is selected.

$$p = \frac{RT}{v-b} - \frac{a(T)}{v(v+b)+b(v-b)} \tag{12}$$

where R represents the gas constant and v is the specific volume, while a and b account for the effects of intermolecular forces.

3.3. Transport properties

The evaluations of thermal conductivity and dynamic viscosity take into account the particular behavior of these quantities at the critical point [55].

The dynamic viscosity of Eq. (13) results from a dilute gas contribution and a residual component, representing a departure from an ideal gas. The dilute gas contribution, μ^0, is given by Eq. (14), while the residual component of viscosity, μ^r, is represented in Eq. (16). Ω represents the collision integral [Eq. (15)], M is the molar mass, and σ is the Lennard–Jones size parameter, while τ and δ represent the reduced density and temperature, respectively. The remaining parameters are tabulated constants [55].

$$\mu = \mu^0(T) + \mu^r(\tau,\delta) \tag{13}$$

$$\mu^0(t) = \frac{0.0266958\sqrt{MT}}{\sigma^2\Omega(T^*)} \tag{14}$$

$$\Omega(T^*) = \exp\left(\sum_{i=0}^{4} b_i\left[\ln(T^*)\right]^i\right) \tag{15}$$

$$\mu^r(\tau,\delta) = \sum_{i=1}^{n} N_i\tau^{t_i}\delta^{d_i}\exp\left(-\gamma_i\delta^{l_i}\right) \tag{16}$$

The variation of viscosity at pressure levels corresponding to the target experimental conditions [12] is shown in Fig. 3. It can be seen that the pressure level of 4 MPa (the critical point of nitrogen) still holds some influence, although this becomes less pronounced as the pressure increases further.

The thermal conductivity of Eq. (17) results from a dilute gas contribution representing ideal gas (λ^0), a residual contribution (λ^r), and a third component representing the singular behavior of thermal conductivity in the vicinity of the critical point, designated "critical enhancement." (λ^c) While the first two components are defined similarly to the dynamic viscosity [55], the critical enhancement is introduced to deal with the critical point singularity [56].

$$\lambda = \lambda^0(T) + \lambda^r(\tau,\delta) + \lambda^c(\tau,\delta) \tag{17}$$

In Eqs. (18) and (19), the additional parameters represent tabulated constants,[55] while in Eq. (20), Ω is a consequence of the specific heat at constant pressure and volume.

$$\lambda^0(T) = N_1\left[\frac{\mu^0(T)}{1\mu\text{Pa}\cdot\text{s}}\right] + N_2\tau^{t_2} + N_3\tau^{t_3} \tag{18}$$

$$\lambda^r(\tau,\delta) = \sum_{i=1}^{n} N_i\tau^{t_i}\delta^{d_i}\exp\left(-\gamma_i\delta^{l_i}\right) \tag{19}$$

$$\lambda^c = \rho c_p\frac{\kappa R_0 T}{6\pi\xi\mu(T,\rho)}\left(\tilde{\Omega}-\tilde{\Omega}_0\right) \tag{20}$$

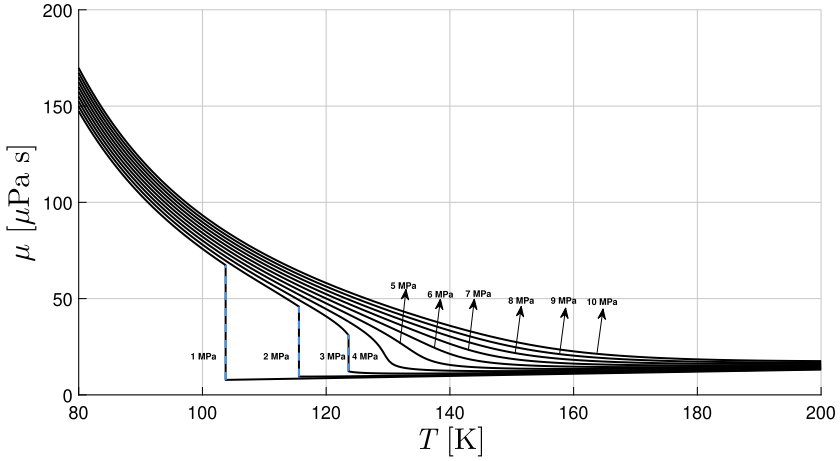

Fig. 3. Plots of viscosity for nitrogen from 1 MPa to 10 MPa, with data from the NIST database [50] (dashed lines represent liquid–vapor discontinuity).

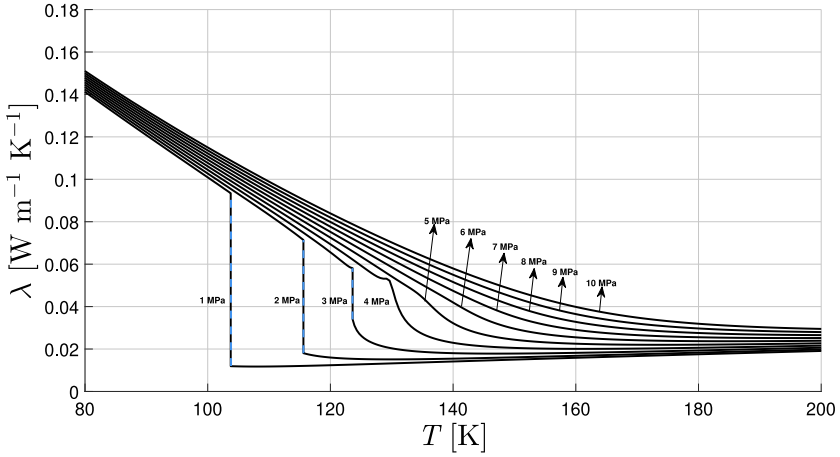

Fig. 4. Plots of thermal conductivity for nitrogen from 1 MPa to 10 MPa, with data from the NIST database (dashed lines represent liquid–vapor discontinuity).

Fig. 4 depicts the evolution of thermal conductivity for the pressure levels considered. It can be seen that the effect of the critical point is much more pronounced than for the viscosity, as indicated by the 4 MPa line. As such, the computational model could benefit from the inclusion of a critical enhancement component to predict the thermal conductivity.

The evaluation of thermodynamic properties such as enthalpy resorts t the departure function formalism, i.e., calculating an ideal low-pressure state and correcting with a departure function to account for high-pressure effects dependent upon the EoS used.

3.4. Numerical algorithm

A finite volume method is used to store scalar values at the cell centers. Diffusive terms in the governing equations are discretized following a second-order central scheme, while advective terms are discretized using the QUICK scheme [57]. In this way, the appearance of non-physical spurious pressure oscillations is mitigated by the inclusion of first-order upwinding. This is especially true when a second-order central scheme is applied to the description of advective fluxes when the grid Péclet number is greater than two, i.e., advection has twice the magnitude of diffusion. The QUICK scheme allows the combination of high-order accuracy with the direction behavior of upwind schemes, providing additional stability for the advective terms in coarser meshes.

A staggered grid configuration is used to ensure that the well-known odd–even decoupling of pressure and velocity does not happen, i.e., that pressure and velocity do not affect each other. Velocity and pressure values are stored in different positions for which the control volumes are no longer equal. Ultimately, the pressure values are calculated directly for the cell face, and no interpolation is needed. This eliminates the decoupling of the pressure and velocity fields, along with any possible oscillations.

High levels of explicit under-relaxation are also used, for which the solutions must be independent. Under-relaxation is applied as follows: first, a high level of under-relaxation is applied to the variables that have reached convergence. A lower level of under-relaxation is then applied, and the iterative solver is re-started for about 100–200 iterations. If the lower under-relaxation has no significant influence on the residuals, the solution is considered independent.

A pressure-based algorithm is implemented in which conservation of mass is implicitly achieved through a pressure-based continuity equation, due to the divergence of momentum and the introduction of $\frac{\partial \bar{\rho}\tilde{u}_i}{\partial x_i} = 0$. The rationale for this algorithm is discussed in the introductory section or in Ref. [43]. Velocity and pressure fields are then obtained simultaneously, followed by energy conservation and the transport of turbulence variables until convergence is reached.

4. Results

4.1. Liquid-like injection

Eventually, both the thermodynamic behavior and the breakup mechanism will play a role in determining the jet structure [2].

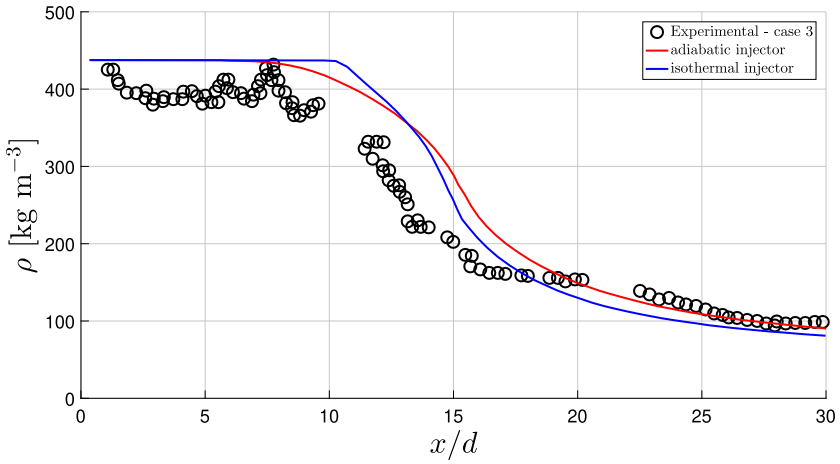

Fig. 5. Axial density distribution for case 3 with adiabatic and isothermal injector wall configurations.

For the liquid-like injection configurations replicated here, the measured injection temperature of the experiments is below the peak in c_p, and so the heating process of the potential core experiences a large density gradient. This is visible in Fig. 1, where small temperature variations produce large density variations. A further indication of the large gradients that occur when crossing the Widom line can be seen through the transport properties of nitrogen, as depicted in Fig. 3 and 4 Fig. 4.

Fig. 5 depicts the results for case 3. Adiabatic and isothermal injector configurations are compared based on their effect on the axial density distribution in the combustion chamber. The experimental data of Mayer et al. [12] are presented for validation purposes, and the axial distance from the injector is normalized by the injector's diameter.

The stabilizing effect of the large density gradient for the liquid-like injection configurations is in accord with more sophisticated LES and DNS solvers [58,59].

In agreement to the mechanical breakup theory, the prediction of a dense potential core is evident in the results. Although the adiabatic injector breakup occurs earlier ($x/d \approx 8$), for the isothermal [2] BCs, a denser core is observed ($x/d \approx 11$). In terms of the core's breakup, we can observe a sharper decrease for the isothermal condition than for the adiabatic case. However, the obtained mean density of $437\,\mathrm{kg\,m^{-3}}$ represents an overprediction with respect to the average of the experimental data. This can be justified by the Raman scattering technique used [12], which leads to underpredicted values for large density values.

The results of Fig. 5 indicate a difference in the mean axial decay between the adiabatic and isothermal injector wall configurations. The difference between both configurations confirms that the thermal breakup introduced by Banuti and Hannemann [2] plays a role in the jet evolution, even though the jet does not receive enough energy to transition across the c_p-Widom line, as it happens in other cases studied.

Another possible interpretation for the longer potential core obtained in the isothermal configuration could be related with the structural nature of eddy viscosity models. Attempts to quantify the structural uncertainty of turbulence models, either by performing sensitivity studies on the calibration constants [23], attempting to develop additional formulations with improved performance [60], or explicitly quantifying the uncertainty levels [61,62], is a research topic that is of increasing interest.

Eddy viscosity models produce an initial low mixing rate [60], which leads to the formation of a longer potential core, something that is visible in Fig. 5. Further downstream, the mixing rate is higher, underpredicting the experimental data. Magalhães et al. [27] compared the performance of several eddy viscosity models, but employed a second-order closure that is not based on Boussinesq's eddy viscosity

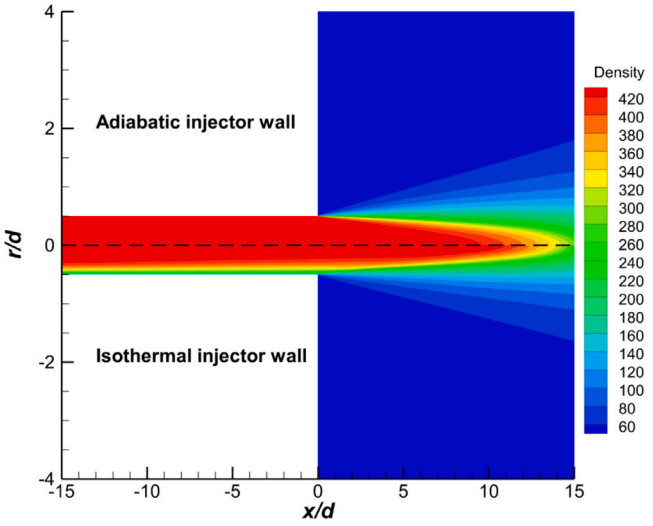

Fig. 6. Density field for case 3 with adiabatic (top) and isothermal (bottom) injector wall configurations.

concept. Under these experimental conditions, we observed that the second-order closure led to an even longer potential core than with the turbulence model of Launder and Spalding [51]. However, in the downstream region, some underprediction of the experimental data was corrected by the second-order closure. This means that the longer potential core does not result from the uncertainties associated with eddy viscosity models, but as a consequence of the level of pseudo-boiling, which requires the system to receive more energy in order to increase the temperature [2,10].

The influence of the thermal effects can be further visualized in Fig. 6 in terms of the dimensionless axial and radial distribution of density, where r is the radial distance taken from the jet's centerline. The small influence of thermal effects leads to different breakup times for the potential core of the jet.

Fig. 7 compares cases 3 and 7 in the isothermal injector configuration. According to Table 1, the difference between these cases is that case 7 occurs at a higher pressure, with less influence from pseudo-boiling (Fig. 1). The results indicate better agreement between the experimental data and our numerical predictions than for case 3. The better performance of the model is visible when comparing cases 3 and 7 in terms of the length of the potential core and the downstream mixing rates. While turbulence model uncertainty plays a role in the

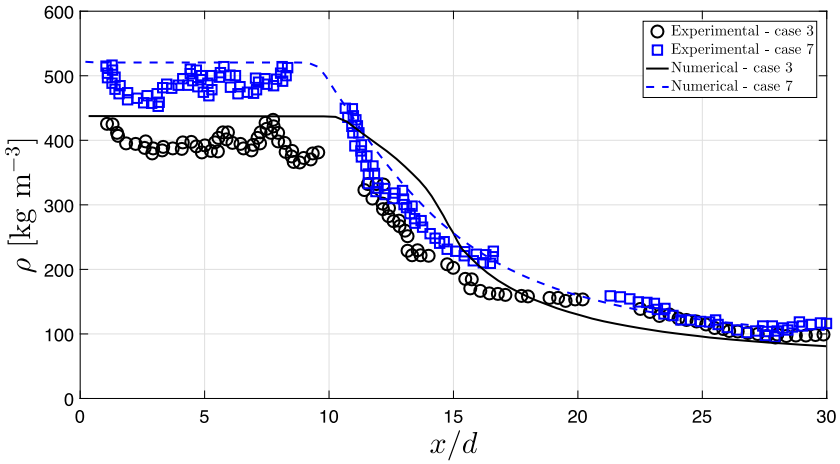

Fig. 7. Axial density distributions for cases 3 and 7 with isothermal injector wall configurations.

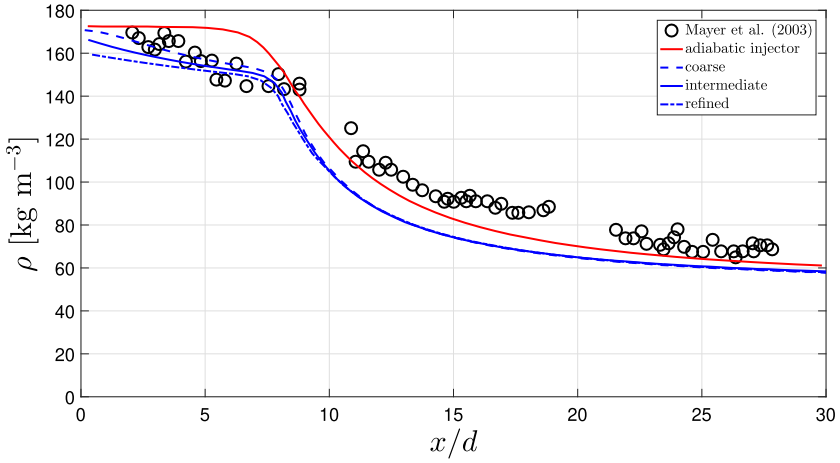

Fig. 8. Axial density distribution for case 4 with adiabatic and isothermal injector wall configurations.

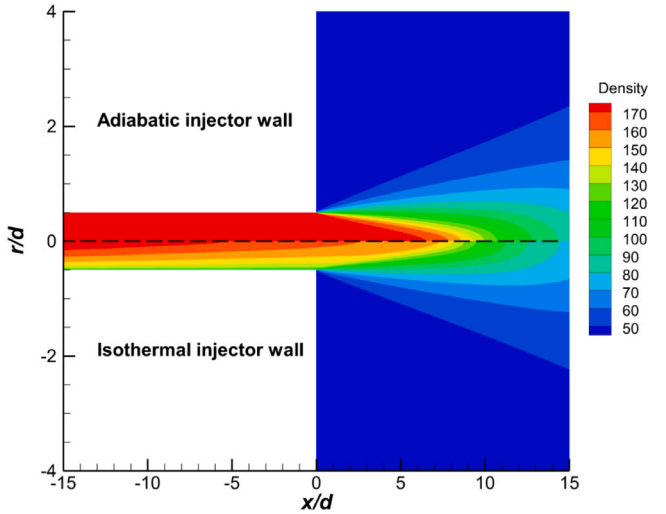

Fig. 9. Axial density distribution for case 4 with adiabatic (top) and isothermal (bottom) injector wall configurations.

interpretation of the results, the key is the ability to accurately capture the effects of pseudo-boiling.

Generally, a closer agreement between experimental data is found for case 7 than for case 3. Looking to Fig. 1, it is possible to observe that case 3 would be the one most affected by uncertainties in the injection temperature, given the steepest slope of the density curve in this region (4 MPa). In comparison uncertainties in the injection temperature for case 7 would play a less preponderant role, given that the slope in density is not as steep.

4.2. Gas-like injection

As previously described, there are structural differences between jets in liquid- and gas-like conditions.

Fig. 8 presents a comparison between adiabatic and isothermal injector wall configurations for experimental case 4 under gas-like injection, therefore taking place after the Widom line has been crossed.

The grid independence was studied with three different refinement levels to ensure that the grid resolution did not influence the results. As depicted in Fig. 8, the axial density distribution, corresponding to the experimental case 4 from Ref. [12], was selected for the independence study.

Fig. 8 depicts the grid independence results for a coarse mesh with 180 000 points, an intermediate mesh with 280 000 nodes, and a refined mesh with 495 000 nodes. As no variation in the slope of the

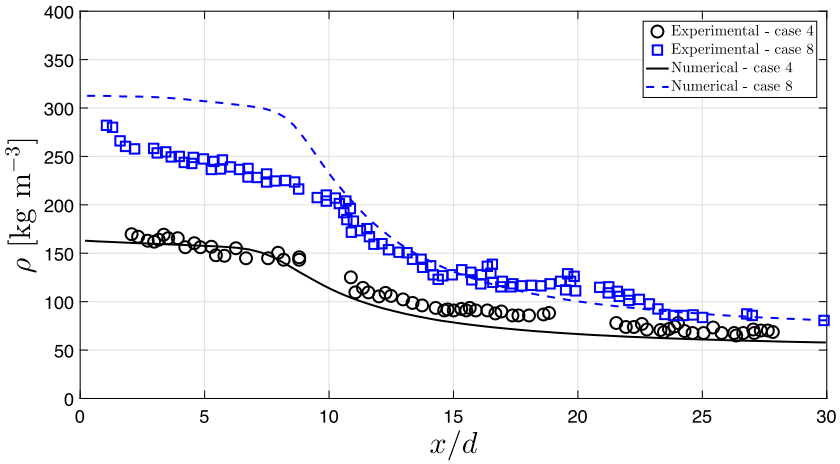

Fig. 10. Axial density distributions for cases 4 and 8 with isothermal injector wall configurations.

results can be distinguished, we concluded that grid independence had been achieved with the intermediate grid.

For the case of the adiabatic injector walls, a potential core can be observed until $x/d \approx 8$, in contrast to the experimental data. Experimentally, no potential core exists; instead, a disintegrated core is present. Nevertheless, there is good agreement between the numerical predictions and the experiment after $x/d \approx 10$.

The disintegrated core is only present when isothermal conditions are considered at the injector walls [2]. A transitional region can be observed at $x/d \approx 8$, after which the jet evolution is dominated by the conditions present inside the combustion chamber. Comparing these results with the liquid-like injection considered in the previous section, we can see that the jet evolution is dominated by the conditions in the chamber to a greater and faster degree under gas-like conditions, since enough energy has already been supplied to the system for a transition across the c_p-Widom line.

By analyzing the density contours for case 4 in Fig. 9, differences in the cases of adiabatic and isothermal BCs are clearly visible. The stratification of density is only seen in the isothermal configuration, resulting in lower density values along the jet's centerline. This is why the density values are different, even at $x/d = 0$ (Fig. 8), as such plug-flow profiles of density cannot be used at the entrance to the combustion chamber. These profiles contribute to an altered jet state at both liquid- and gas-like, with a more profound impact on gas-like injection phenomena. Through these results, we are able to support and extend the conclusions reached by Banuti and Hannemann [2] for a broad range of experimental conditions.

Even though closer agreement is achieved for the initial gas-like configuration than for the liquid-like case, a comparison is also performed for higher-pressure conditions at a supercritical state. Fig. 10 compares experimental cases 4 and 8. Once again, there is a striking difference between the higher pressure of case 8 in comparison to case 4. The increased pressure results in higher density values for case 8, and as such, the same problem of underpredictions of the experimental results, arising from the Raman scattering technique, is observed in the comparison of the disintegrated core. For the remaining jet evolution, starting at $x/d \approx 10$ until the end of the available experimental data at $x/d \approx 30$, the numerical predictions match the experimental data.

The numerical results over-prediction in relation to the experiments observed in Fig. 10 for case 8 until $x/d = 10$ could be related to the compressibility Widom line [7], mentioned in the introduction. Similarly to Soret and Dufour effects, compressibility effects [63] not encountered in low-pressure jets could lead to different coupling mechanisms in the Widom region. However, the inclusion of additional terms in the turbulence model is not a straightforward process [23], made more difficult due to the restricted amount of experimental data.

Overall, from the agreement found in the numerical results presented here, the numerical solver proposed in this paper is suitable for describing liquid- and gas-like supercritical injection phenomena. Future work will investigate how to better incorporate and more accurately replicate pseudo-boiling effects.

5. Conclusions

This paper describes the use of a RANS method to predict trans- and supercritical fluid behavior. Liquid- and gas-like injection conditions were analyzed, accounting for both adiabatic and isothermal injector wall BCs. Both the injector and combustion chamber were considered in the computational domain.

The accurate description of supercritical fluid behavior relies on both mechanical and thermal breakup mechanisms. For liquid-like injection configurations, corresponding to transcritical conditions, dense potential cores are retrieved, whereas disintegrated cores provide a stronger evidence of the thermal breakup under gas-like conditions. The concept of thermal breakup proposed in the literature is of central importance, and through it insights into supercritical jet behavior were achieved. As a result, the plug-flow profiles that are sometimes considered provide an incorrect representation of the flow physics, as shown in the density contours at the chamber entrance.

Furthermore, it was demonstrated that isothermal BCs are in accord with the experimental values for jet behavior. Considering different levels of pseudo-boiling, it was possible to demonstrate the influence of this phenomenon on the jet evolution.

The results suggest that the liquid-like configurations are similar in terms of jet stabilization. However, the isothermal injector contributes to a longer stabilization of the potential core under transcritical conditions.

Declaration of competing interest

The authors declare that they have no known competing financial interests or personal relationships that could have appeared to influence the work reported in this paper.

Acknowledgments

The present work was performed under the scope of activities at the Aeronautics and Astronautics Research Center (AEROG) of the Laboratório Associado em Energia, Transportes e Aeronáutica (LAETA), and was supported by the Fundação para a Ciência e Tecnologia, Portugal (Grant No. SFRH/BD/136381/2018, Project No. UIDB/50022/2020). The authors would like to recognize the comments from the two anonymous reviewers during the peer review process.

References

[1] D.T. Banuti, M. Raju, C. Ma, M. Ihme, J. Hickey, Seven questions about supercritical fluids – towards a new fluid state diagram, in: 55th AIAA Aerospace Sciences Meeting, (AIAA 2017-1106) 2017, http://dx.doi.org/10.2514/6.2017-1106.

[2] D.T. Banuti, K. Hannemann, The absence of a dense potential core in supercritical injection: A thermal break-up mechanism, Phys. Fluids 28 (3) (2016) 035103, http://dx.doi.org/10.1063/1.4943038.

[3] M. Oschwald, J.J. Smith, R. Braman, J. Hussong, A. Schik, B. Chehroudi, D.G. Talley, Injection of fluids into supercritical environments, Combust. Sci. Technol. 178 (1–3) (2006) 49–100, http://dx.doi.org/10.1080/00102200500292464.

[4] B. Chehroudi, Recent experimental efforts on high-pressure supercritical injection for liquid rockets and their implications, Int. J. Aerosp. Eng. 2012 (2012) 1–31, http://dx.doi.org/10.1155/2012/121802.

[5] C. Lagarza-Cortés, J. Ramírez-Cruz, M. Salinas-Vázquez, W. V.-Rodríguez, J. Cubos-Ramírez, Large-Eddy simulation of transcritical and supercritical jets immersed in a quiescent environment, Phys. Fluids 31 (2) (2019) 025104, http://dx.doi.org/10.1063/1.5054797.

[6] T. Schmitt, L. Selle, B. Cuenot, T. Poinsot, Large-Eddy simulation of transcritical flows, C. R. Mec. 337 (2009) 528–538, http://dx.doi.org/10.1016/j.crme.2009.06.022.

[7] A.R. Imre, C. Ramboz, U.K. Deiters, T. Kraska, Anomalous fluid properties of carbon dioxide in the supercritical region: Application to geological CO2 storage and related hazards, Environ. Earth Sci. 73 (8) (2014) 4373–4384, http://dx.doi.org/10.1007/s12665-014-3716-5.

[8] F.A. Gorelli, T. Bryk, M. Krisch, G. Ruocco, M. Santoro, T. Scopigno, Dynamics and thermodynamics beyond the critical point, Sci. Rep. 3 (1) (2013) http://dx.doi.org/10.1038/srep01203.

[9] V. Gerber, S. Baab, F.J. Förster, H. Mandler, B. Weigand, G. Lamanna, Fluid injection with supercritical reservoir conditions: Overview on morphology and mixing, J. Supercrit. Fluids 169 (2021) 105097, http://dx.doi.org/10.1016/j.supflu.2020.105097.

[10] D.T. Banuti, Crossing the widom-line – supercritical pseudo-boiling, J. Supercrit. Fluids 98 (2015) 12–16, http://dx.doi.org/10.1016/j.supflu.2014.12.019.

[11] M. Oschwald, A. Schik, Supercritical nitrogen free jet investigated by spontaneous Raman scattering, Exp. Fluids 27 (1999) 497–506, http://dx.doi.org/10.2514/6.1999-2887.

[12] W. Mayer, J. Telaar, R. Branam, G. Schneider, J. Hussong, Raman measurements of cryogenic injection at supercritical pressure, Heat Mass Transf. 39 (8–9) (2003) 709–719, http://dx.doi.org/10.1007/s00231-002-0315-x.

[13] M. Habiballah, M. Orain, F. Grisch, L. Vingert, P. Gicquel, Experimental studies of high-pressure cryogenic flames on the Mascotte facility, Combust. Sci. Technol. 178 (1–3) (2006) 101–128, http://dx.doi.org/10.1080/00102200500294486.

[14] S. Dowy, A. Braeuer, K. Reinhold-López, A. Leipertz, Laser analyses of mixture formation and the influence of solute on particle precipitation in the SAS process, J. Supercrit. Fluids 50 (3) (2009) 265–275, http://dx.doi.org/10.1016/j.supflu.2009.06.018.

[15] A. Roy, C. Segal, Experimental study of fluid jet mixing at supercritical conditions, J. Propuls. Power 26 (6) (2010) 1205–1211, http://dx.doi.org/10.2514/1.48462.

[16] A. Roy, C. Joly, C. Segal, Disintegrating supercritical jets in a subcritical environment, J. Fluid Mech. 717 (2013) 193–202, http://dx.doi.org/10.1017/jfm.2012.566.

[17] D. Bassing, A.S. Braeuer, The lag between micro- and macro-mixing in compressed fluid flows, Chem. Eng. Sci. 163 (2017) 105–113, http://dx.doi.org/10.1016/j.ces.2017.01.034.

[18] L. Selle, G. Ribert, Modeling requirements for large-Eddy simulation of turbulent flows under supercritical thermodynamics conditions, Cen. Turbul. Res. Proc. Summer Programme 2008 (2008).

[19] J. Bellan, Supercritical (and subcritical) fluid behavior and modeling: Drops, streams, shear and mixing layers, jets and sprays, Prog. Energy Combust. Sci. 26 (4–6) (2000) 329–366, http://dx.doi.org/10.1016/S0360-1285(00)00008-3.

[20] N. Okong'o, J. Bellan, Perturbation and initial Reynolds number effects on transition attainment of supercritical, binary, temporal mixing layers, Comput. Fluids 33 (8) (2004) 1023–1046, http://dx.doi.org/10.1016/j.compfluid.2003.10.001.

[21] J. Bellan, Theory, modeling and analysis of turbulent supercritical mixing, Combust. Sci. Technol. 178 (1–3) (2006) 253–281, http://dx.doi.org/10.1080/00102200500292241.

[22] U. Unnikrishnan, X. Wang, S. Yang, V. Yang, Subgrid scale modeling of the equation of state for turbulent flows under supercritical conditions, in: 53rd AIAA/SAE/ASEE Joint Propulsion Conference, (AIAA 2017-4855) 2017, http://dx.doi.org/10.2514/6.2017-4855.

[23] H. Xiao, P. Cinnella, Quantification of model uncertainty in RANS simulations: A review, Prog. Aerosp. Sci. 108 (2019) 1–31, http://dx.doi.org/10.1016/j.paerosci.2018.10.001.

[24] P. Sagaut, Large Eddy Simulation for Incompressible Flows, in: Scientific Computation, Springer, ISBN: 9783540437536, 2001.

[25] X. Petit, G. Ribert, G. Lartigue, P. Domingo, Large Eddy simulation of supercritical fluid injection, J. Supercrit. Fluids 84 (2013) 61–73, http://dx.doi.org/10.1016/j.supflu.2013.09.011.

[26] A. Gnanaskandan, J. Bellan, Large Eddy simulations of high-pressure jets: Effect of subgrid scale modeling, in: 55th AIAA Aerospace Sciences Meeting, (AIAA 2017-1105) 2017, http://dx.doi.org/10.2514/6.2017-1105.

[27] L. Magalhães, F. Carvalho, A. Silva, J. Barata, Turbulence modeling insights into supercritical nitrogen mixing layers, Energies 13 (7) (2020) 1586, http://dx.doi.org/10.3390/en13071586.

[28] P.C. Ma, Y. Lv, M. Ihme, An entropy-stable hybrid scheme for simulations of transcritical real-fluid flows, J. Comput. Phys. 340 (2017) 330–357, http://dx.doi.org/10.1016/j.jcp.2017.03.022.

[29] B.M. Ningegowda, F. Rahantamialisoa, J. Zembi, A. Pandal, H.G. Im, M. Battistoni, Large Eddy simulations of supercritical and transcritical jet flows using real fluid thermophysical properties, SAE Tech. Paper Ser. (2020) http://dx.doi.org/10.4271/2020-01-1153.

[30] J. Barata, I. Gökalp, A. Silva, Numerical study of cryogenic jets under supercritical conditions, J. Propuls. Power 19 (1) (2003) 142–147, http://dx.doi.org/10.2514/2.6090.

[31] P.C. Ma, H. Wu, D.T. Banuti, M. Ihme, Numerical analysis on mixing processes for transcritical real-fluid simulations, in: 2018 AIAA Aerospace Sciences Meeting, (AIAA 2018-1813) 2018, http://dx.doi.org/10.2514/6.2018-1813.

[32] M.T. Migliorino, J.-B. Chapelier, C. Scalo, G. Lodato, Assessment of spurious numerical oscillations in high-order spectral difference solvers for supercritical flows, in: 2018 Fluid Dynamics Conference, (AIAA 2018-4273) 2018, http://dx.doi.org/10.2514/6.2018-4273.

[33] G. Lacaze, T. Schmitt, A. Ruiz, J.C. Oefelein, Comparison of energy-, pressure- and enthalpy-based approaches for modeling supercritical flows, Comput. Fluids 181 (2019) 35–56, http://dx.doi.org/10.1016/j.compfluid.2019.01.002.

[34] J. Sierra-Pallares, J.G. del Valle, P. Garcia-Carrascal, F.C. Ruiz, Numerical study of supercritical and transcritical injection using different turbulent Prandtl numbers. A second law analysis, J. Supercrit. Fluids 115 (2016) 86–98, http://dx.doi.org/10.1016/j.supflu.2016.05.001.

[35] F. Ries, J. Janicka, A. Sadiki, Thermal transport and entropy production mechanisms in a turbulent round jet at supercritical thermodynamic conditions, Entropy 19 (2017) 404, http://dx.doi.org/10.3390/e19080404.

[36] F. Ries, D. Kütemeier, Y. Li, K. Nishad, A. Sadiki, Effect chain analysis of supercritical fuel disintegration processes using an LES-based entropy generation analysis, Combust. Sci. Technol. 192 (11) (2020) 2171–2188, http://dx.doi.org/10.1080/00102202.2020.1770239.

[37] T. Kim, Y. Kim, S. Kim, Numerical study of cryogenic liquid nitrogen jets at supercritical pressures, J. Supercrit. Fluids 56 (2) (2011) 152–163, http://dx.doi.org/10.1016/j.supflu.2010.12.008.

[38] T.S. Park, LES and RANS simulations of cryogenic liquid nitrogen jets, J. Supercrit. Fluids 72 (2012) 232–247, http://dx.doi.org/10.1016/j.supflu.2012.09.004.

[39] S. Kawai, Y. Oikawa, Turbulence modeling for turbulent boundary layers at supercritical pressure: A model for turbulent mass flux, Flow Turbul. Combust. 104 (2–3) (2019) 625–641, http://dx.doi.org/10.1007/s10494-019-00079-z.

[40] T.S. Park, Application of k-ϵ turbulence models with density corrections to variable density jets under subcritical/supercritical conditions, Numer. Heat Transfer 77 (2) (2019) 162–178, http://dx.doi.org/10.1080/10407782.2019.1685817.

[41] T. Schmitt, L. Selle, A. Ruiz, B. Cuenot, Large-Eddy simulation of supercritical-pressure round jets, AIAA J. 48 (9) (2010) 2133–2144, http://dx.doi.org/10.2514/1.J050288.

[42] T. Schmitt, A. Ruiz, L. Selle, B. Cuenot, Numerical investigation of destabilization of supercritical round turbulent jets using large Eddy simulation, Prog. Propuls. Phys. 2 (2011) 225–238, http://dx.doi.org/10.1051/eucass/201102225.

[43] M. Jarczyk, M. Pfitzner, Large Eddy simulation of supercritical nitrogen jets, in: 50th AIAA Aerospace Sciences Meeting Including the New Horizons Forum and Aerospace Exposition, (AIAA 2012-1270) 2012, http://dx.doi.org/10.2514/6.2012-1270.

[44] H. Müller, C.A. Niedermeier, M. Jarczyk, M. Pfitzner, S. Hickel, N.A. Adams, Large Eddy simulation of trans- and supercritical injection, Prog. Propuls. Phys. 8 (2016) 5, http://dx.doi.org/10.1051/eucass/201608005.

[45] F. Ries, P. Obando, I. Shevchuck, J. Janicka, A. Sadiki, Numerical analysis of turbulent flow dynamics and heat transport in a round jet at supercritical conditions, Int. J. Heat Fluid Flow 66 (2017) 172–184, http://dx.doi.org/10.1016/j.ijheatfluidflow.2017.06.007.

[46] P.E. Lapenna, F. Creta, Direct numerical simulation of transcritical jets at moderate Reynolds number, AIAA J. 57 (6) (2019) 2254–2263, http://dx.doi.org/10.2514/1.J058360.

[47] B. Chehroudi, D. Talley, E. Coy, Visual characteristics and initial growth rates of round cryogenic jets at subcritical and supercritical pressures, Phys. Fluids 14 (2) (2002) 850–861, http://dx.doi.org/10.1063/1.1430735.

[48] J. Bellan, Future challenges in the modelling and simulations of high-pressure flows, Combust. Sci. Technol. 192 (7) (2020) 1199–1218, http://dx.doi.org/10.1080/00102202.2020.1719404.

[49] P.E. Lapenna, Characterization of pseudo-boiling in a transcritical nitrogen jet, Phys. Fluids 30 (7) (2018) 77–106, http://dx.doi.org/10.1063/1.5038674.

[50] P. Linstrom, W. Mallard (Eds.), NIST Chemistry WebBook, NIST Standard Reference Database 69, National Institute of Standards and Technology, 1997, http://dx.doi.org/10.18434/T4D303.
[51] B.E. Launder, D.B. Spalding, Lectures in mathematical models of turbulence, 1972, Academic Press, London, UK.
[52] D. Peng, D.B. Robinson, A new two-constant equation of state, Ind. Eng. Chem. Fundam. 15 (1) (1976) 59–64, http://dx.doi.org/10.1021/i160057a011.
[53] G. Soave, Equilibrium constants from a modified Redlich–Kwong equation of state, Chem. Eng. Sci. 27 (6) (1972) 1197–1203, http://dx.doi.org/10.1016/0009-2509(72)80096-4.
[54] D.T. Banuti, K. Hannemann, Real gas library in continuous phase propellant injection model for liquid rocket engines, in: 49th AIAA/ASME/SAE/ASEE Joint Propulsion Conference, (AIAA 2013-4068) 2013, http://dx.doi.org/10.2514/6.2013-4068.
[55] E.W. Lemmon, R.T. Jacobsen, Viscosity and thermal conductivity equations for nitrogen, oxygen, argon and air, Int. J. Thermophys. 25 (1) (2004) 21–69, http://dx.doi.org/10.1023/B:IJOT.0000022327.04529.f3.
[56] G.A. Olchowy, J.V. Sengers, A simplified representation for the thermal conductivity of fluids in the critical region, Int. J. Thermophys. 10 (2) (1989) 417–426, http://dx.doi.org/10.1007/BF01133538.
[57] B.P. Leonard, A stable and accurate convective modelling procedure based on quadratic upstream interpolation, Comput. Methods Appl. Mech. Engrg. 19 (1) (1979) 59–98, http://dx.doi.org/10.1016/0045-7825(79)90034-3.
[58] R. Miller, K. Harstad, J. Bellan, Direct numerical simulations of supercritical fluid mixing layers applied to heptane–nitrogen, J. Fluid Mech. 436 (2001) 1–39, http://dx.doi.org/10.1017/S0022112001003895.
[59] J.C. Oefelein, Thermophysical characteristics of shear-coaxial LOX–H2 flames at supercritical pressure, Proc. Combust. Inst. 30 (2) (2005) 2929–2937, http://dx.doi.org/10.1016/j.proci.2004.08.212.
[60] N.J. Georgiadis, D.A. Yoder, W.A. Engblom, Evaluation of modified two-equation turbulence models for jet flow predictions, AIAA J. 44 (12) (2006) 3107–3114, http://dx.doi.org/10.2514/1.22650.
[61] A.A. Mishra, G. Iaccarino, Uncertainty estimation for Reynolds-averaged Navier–Stokes predictions of high-speed aircraft nozzle jets, AIAA J. 55 (11) (2017) 3999–4004, http://dx.doi.org/10.2514/1.J056059.
[62] L. Cook, A. Mishra, J. Jarrett, K. Willcox, G. Iaccarino, Optimization under turbulence model uncertainty for aerospace design, Phys. Fluids 31 (10) (2019) 105111, http://dx.doi.org/10.1063/1.5118785.
[63] M. Rubesin, Extra compressibility terms for the favre–averaged two–equation models of inhomogeneous turbulent flows, Tech. Rep, (177556) NASA, 1990.